Noble-Metal-Free Electrocatalysts

Deutsche Ausgabe: DOI: 10.1002/ange.201600850
Internationale Ausgabe: DOI: 10.1002/anie.201600850

Two-Dimensional Core-Shelled Porous Hybrids as Highly Efficient Catalysts for the Oxygen Reduction Reaction

Kai Yuan[+], Xiaodong Zhuang[+], Haiyan Fu, Gunther Brunklaus, Michael Forster, Yiwang Chen, Xinliang Feng, and Ullrich Scherf**

Abstract: *Two-dimensional (2D) transition-metal dichalcogenides (TMDs) have drawn much attention due to their unique physical and chemical properties. Using TMDs as templates for the generation of 2D sandwich-like materials with remarkable properties still remains a great challenge due to their poor solvent processability. Herein, MoS_2-coupled sandwich-like conjugated microporous polymers (M-CMPs) with high specific surface area were successfully developed by using functionalized MoS_2 nanosheets as template. As-prepared M-CMPs were further used as precursors for preparation of MoS_2-embedded nitrogen-doped porous carbon nanosheets, which were revealed as novel electrocatalysts for oxygen reduction reaction with mainly four-electron transfer mechanism and ultralow half-wave potential in comparison with commercial Pt/C catalyst. Our strategy to core–shelled sandwich-like hybrids paves a way for a new class of 2D hybrids for energy conversion and storage.*

Graphene as the best-known two-dimensional (2D) nanomaterial has been intensively studied since 2004 due to its exceptional physical and chemical properties.[1] Covalent functionalization of graphene has been demonstrated as a viable approach for tailoring the electronic and chemical properties of graphene-based materials, enabling the introduction of reactive groups for subsequent functionalization.[2] Functionalized graphenes are promising templates for the construction of 2D hybrid materials, such as 2D metal oxides, metal sulfides, carbon nanosheets, and microporous polymer hybrids.[3] Beyond graphene, more and more other 2D nanomaterials attracted tremendous attentions in recent years.[4] Among these 2D materials, transition-metal dichalcogenides (TMDs) such as MoS_2, WS_2, $MoSe_2$ and WSe_2 are one of the primary focuses of research.[5] Because of their unique electronic, mechanical, optical and chemical properties, TMDs showed high application potential in electronic devices and for catalysis and energy storage.[4a] The covalent functionalization of TMDs can further enhance the versatility of 2D TMDs.[6] For example, improving the solubility in common solvents facilitates their integration into polymer matrices.[7] Furthermore, entirely new materials can be designed by attaching functional ligands.[8] In contrast to graphene, reports on the covalent functionalization of TMDs remain scarce.[6,7,9] Up to now, only a few covalently connected polymer/MoS_2 hybrids have been reported.[6,8,10]

Ultrathin MoS_2 nanosheets are excellent candidates for constructing hybrids with high specific surface area and high flexibility.[3b,11] Both sides of the MoS_2 nanosheets can be used as templates for the growth of functional composites with sandwich-like structure.[3b,11b] Heteroatom-doped carbons as promising materials for catalysis or energy conversion and storage have attracted growing attention due to their unique structural and electronic properties.[12] Conjugated microporous polymers (CMPs) with high specific surface area and hierarchical pore distribution are favored for a controllable construction of carbon-based materials.[3d,13] Heteroatoms can be controllably introduced into CMPs network via heteroatom-containing tectons (building blocks).[14] In this regard, the combination of MoS_2 nanosheets and CMPs may generate 2D hybrid sandwiches for applications in catalysis and electrochemical energy-related devices. However, using MoS_2 as templates for the generation of 2D sandwich-like materials with remarkable properties still remains a great challenge due to their poor solvent processability.

Herein, we demonstrate the fabrication of MoS_2-templated conjugated microporous polymer (M-CMP) nanosheets by growing nitrogen-rich CMPs on 4-iodophenyl-functionalized MoS_2 templates. Unique polymer/MoS_2 sandwiches with high specific surface area and hierarchically porous structure were achieved. As-prepared 2D porous polymer/MoS_2 sandwiches can be further converted into the corresponding 2D porous carbon hybrids by direct pyrolysis of the M-CMP nanosheets. As proof-of-concept, oxygen reduction reaction (ORR) and supercapacitor performances were studied. The strong interaction between nitrogen-doped

[*] K. Yuan,[+] Dr. M. Forster, Prof. Dr. U. Scherf
Macromolecular Chemistry Group (buwmakro) and Institute for Polymer Technology, Bergische Universität Wuppertal
Gauss-Str. 20, 42119 Wuppertal (Germany)
E-mail: scherf@uni-wuppertal.de
Dr. X. Zhuang,[+] Prof. Dr. X. Feng
Center for Advancing Electronics Dresden (cfaed) and Department of Chemistry and Food Chemistry, Technische Universität Dresden
Mommsenstrasse 4, 01062 Dresden (Germany)
E-mail: xinliang.feng@tu-dresden.de
H. Fu, Prof. Dr. Y. Chen
College of Chemistry/Institute of Polymers, Nanchang University
999 Xuefu Avenue, Nanchang 330031 (China)
Dr. G. Brunklaus
Institut für Physikalische Chemie
Westfälische Wilhelms-Universität Münster
Corrensstr. 28, 48149 Münster (Germany)
Dr. X. Zhuang[+]
School of Chemistry and Chemical Engineering
Shanghai Jiao Tong University
Dongchuan Road 800, 200240, Shanghai (P.R. China)
[+] These authors contributed equally to this work.

Supporting information for this article can be found under: http://dx.doi.org/10.1002/anie.201600850.

porous carbon and MoS_2 within the sandwich structure boosts the performance for ORR and electrochemical energy storage. As a result, the 2D porous carbon hybrids display a more positive half-wave potential (−0.14 V vs. −0.13 V for Pt/C) and a higher diffusion-limited current (5.4 mA cm^{-2}) in ORR in comparison with MoS_2-free porous carbons derived from CMPs. Moreover, the 2D hybrids deliver high capacitance up to 344 F g^{-1} at 0.2 A g^{-1}, 45% higher than that of corresponding MoS_2-free porous carbons (237 F g^{-1}).

The synthesis strategy for M-CMPs is illustrated in Scheme 1. First, chemically exfoliated MoS_2 (CE-MoS_2) was generated by reacting bulk MoS_2 with *n*-butyllithium (*n*-BuLi). Then, CE-MoS_2 was functionalized with 4-iodophenyl diazonium salt under aqueous conditions (detailed experimental procedures are given in the Supporting Information).[7,9] The obtained 4-iodophenyl-functionalized MoS_2 (MoS_2-I) can be well-dispersed in various organic solvents, such as dimethylformamide (DMF, Figure S1) and toluene. The successful functionalization of MoS_2 was evidenced by several analytical techniques, the results are presented in Figures S1–S7 (for detailed discussions see the Supporting Information). Next, the arylacetylene building block 1,3,5-triethynylbenzene mixed with an aryl di- or trihalide (2,5-dibromopyridine, 2,5-dibromopyrazine, or 2,4,6-trichloro-1,3,5-triazine) was reacted with MoS_2-I in anhydrous DMF in the presence of $Pd(PPh_3)_4$, CuI and Et_3N under inert atmosphere. This Sonogashira–Hagihara reaction was carried out at 100 °C for 3 days under vigorous stirring and yielded insoluble, crude products that were collected by filtration and purified by Soxhlet extraction. Finally, the sandwich-like M-CMPs, denoted as M-CMP1, M-CMP2 and M-CMP3 for the pyridine-, pyrazine- and triazine-containing polymers, respectively, were obtained after vacuum drying. The corresponding conjugated microporous polymers (CMPs), denoted as CMP1, CMP2 and CMP3 for the pyridine-, pyrazine- and triazine-containing polymers, respectively, without the MoS_2 template were also synthesized for comparison by using similar procedure (Scheme S1).

Morphologies and microstructures of the M-CMPs were investigated by scanning electron microscopy (SEM), transmission electron microscopy (TEM), high-resolution TEM (HRTEM) and atomic force microscopy (AFM). All of the M-CMPs display similar sheet-like structures. Therefore, M-CMP2 will be discussed as a typical example. As shown in Figures 1a and 1b, M-CMP2 possesses a wrinkled sheet morphology similar to that of MoS_2 layers. The surface of the M-CMP sandwiches show a similar average roughness as the non-templated CMPs due to the coating of the porous CMPs on MoS_2 (Figure S8). No free CMP particles or "naked" MoS_2 sheets were observed, thus indicating that the majority of the monomers have been grafted onto the MoS_2 surface. In the HRTEM image of M-CMP2, the alternating bright and dark areas may be attributed to the microporous struc-

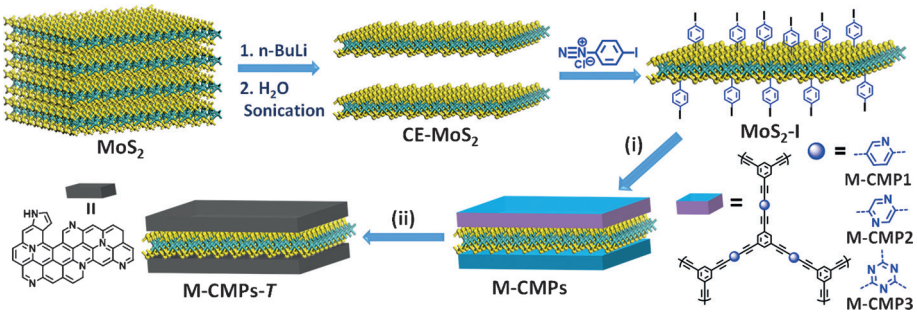

Scheme 1. Idealized formula scheme depicting the chemical exfoliation of bulk MoS_2 and subsequent functionalization with 4-iodophenyl substituents under formation of MoS_2-I as well as the preparation of MoS_2-templated conjugated microporous polymers (M-CMPs) and the corresponding MoS_2/nitrogen-doped porous carbon (M-CMPs-*T*) hybrids. i) monomers: 1,3,5-triethynylbenzene and 2,5-dibromopyridine, 2,5-dibromopyrazine, or 2,4,6-trichloro-1,3,5-triazine, argon, $Pd(PPh_3)_4$, CuI, Et_3N, DMF, 100 °C, 3 days; ii) argon, heating rate: 10 °C min^{-1}, pyrolysis temperature: 700, 800, or 900 °C, 2 h.

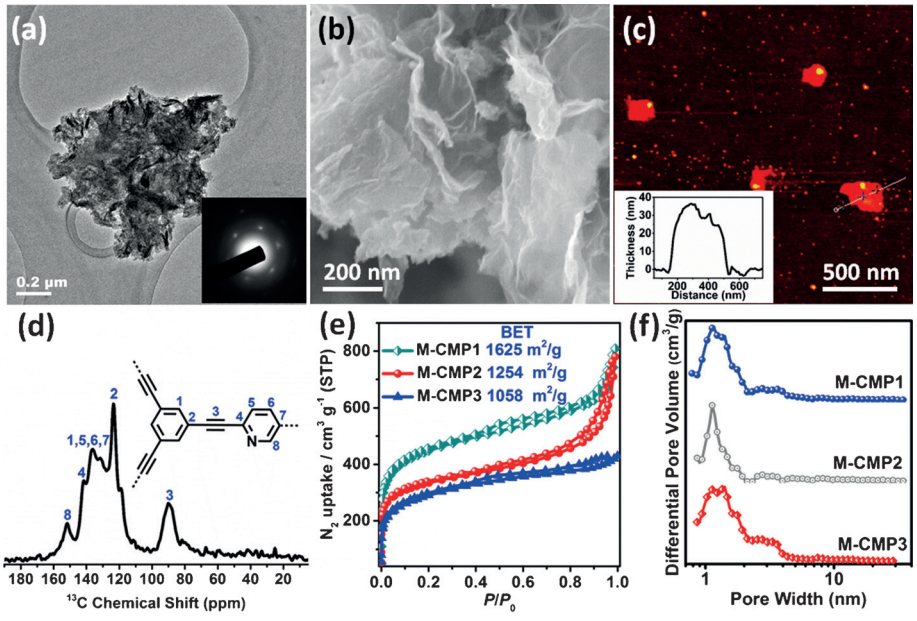

Figure 1. a) TEM, b) SEM, and c) AFM images of M-CMP2. Inset of (a) is the selected-area electron diffraction (SAED) pattern of a M-CMP2 nanosheet. d) Solid-state ^{13}C CP/MAS spectrum of M-CMP1 and its peak assignments. e) Nitrogen adsorption/desorption isotherms, and f) corresponding pore size distribution profiles of M-CMPs.

ture of the M-CMPs with homogenously distributed pores in M-CMPs (Figure S8). AFM and thickness analyses (Figure 1c) indicate the presence of M-CMP sandwiches with a uniform thickness of 35 ± 6 nm. Oppositely, the non-templated CMPs display a granular structure (Figure S9). These results confirm the role of MoS_2-I as template for the growth of the CMPs layers on both sides of MoS_2 sheets.

The chemical structure of the M-CMPs was analyzed by FTIR and solid-state ^{13}C cross-polarization/magic angle spinning nuclear magnetic resonance (CP/MAS NMR) spectroscopy. The disappearance of the C–Br (at 1080 cm^{-1}) and alkynyl C–H (at 3275 cm^{-1}) stretch vibrations in the FTIR spectra of M-CMP1 imply the occurrence of an efficient arylacetylene–aryl coupling (Figure S10). In the ^{13}C NMR spectrum of M-CMP1 the signal at 152 ppm can be assigned to the pyridine carbons in the proximity of the nitrogen atom (Figure 1d). Moreover, diaryl C≡C signals at 88–90 ppm are observed again indicating successful formation of the CMP skeleton on the MoS_2 surface. The FTIR and NMR spectra of M-CMP2 and M-CMP3 (Figures S10 and S11) can be interpreted in similar manner. M-CMPs were further characterized by XPS (Figure S12). All M-CMPs are composed of similar components, C, N, S and Mo, which are summarized in Table S1. All structure characterization data indicate the successful synthesis of microporous MoS_2/polymer hybrid nanosheets by utilizing MoS_2-I as template.

Consequently, nitrogen adsorption/desorption measurements were carried out for investigation of the porous nature of M-CMPs. The nitrogen sorption isotherms and the corresponding pore size distributions of the M-CMPs are presented in Figures 1e,f. All M-CMPs showed reversible type-IV isotherms with BET surface areas of 1625, 1254, and 1058 $m^2 g^{-1}$ for M-CMP1, M-CMP2 and M-CMP3, respectively. The pore size distributions based on non-local density functional theory (NLDFT) method (Figure 1f) indicate the presence of both meso- and micropores in M-CMPs. Notably, M-CMPs show much higher BET surface areas than those for CMPs without MoS_2 (1086, 886 and 392 $m^2 g^{-1}$), respectively (Figures S13 and S14). This may originate from a synergetic effect of the MoS_2 template on the CMP porosity.

CMPs-derived porous carbons with integrated heteroatoms, metal clusters or metal nanoparticles, or metal oxides are promising materials for various applications such as gas storage and separation, energy conversion and storage, or electrochemical catalysis.[3d,13a,b,15] Thermogravimetric analysis (TGA) of M-CMPs revealed that they can be easily transformed into MoS_2/carbon hybrid materials (ca. 80% residual at 800 °C, Figure S15). Therefore, M-CMP1, M-CMP2 and M-CMP3 were pyrolyzed at 700, 800, or 900 °C for 2 h under an argon atmosphere (Scheme 1). The resulting MoS_2/nitrogen-doped porous carbon (M-CMPs-*T*) hybrids are denoted as M-CMP1-*T*, M-CMP2-*T* and M-CMP3-*T*, respectively, in which *T* represents the pyrolysis temperature. For comparison, porous carbons without MoS_2 were also prepared by pyrolysis of the CMPs at *T* °C, denoted as the corresponding CMP*n*-*T* ($n = 1, 2, 3$, $T = 800$), respectively.

The SEM and TEM images of the M-CMPs-*T* hybrids still display the preserved nanosheet morphology (Figures 2a,b and S16). On the contrary, the CMP-derived carbons exhibit a particular morphology (Figure S16). HRTEM image and corresponding SAED pattern of M-CMP2-800 indicate that the porous carbons in close connected with MoS_2 templates (Figure 2c). Scanning transmission electron microscopy (STEM) element mapping images (Figures 2d and S17) clearly show homogeneous distribution of C, N, Mo and S in M-CMP2-800 nanosheets.

After pyrolysis, the obtained MoS_2/porous carbon hybrids still show high BET surface area (790–850 $m^2 g^{-1}$) indicating

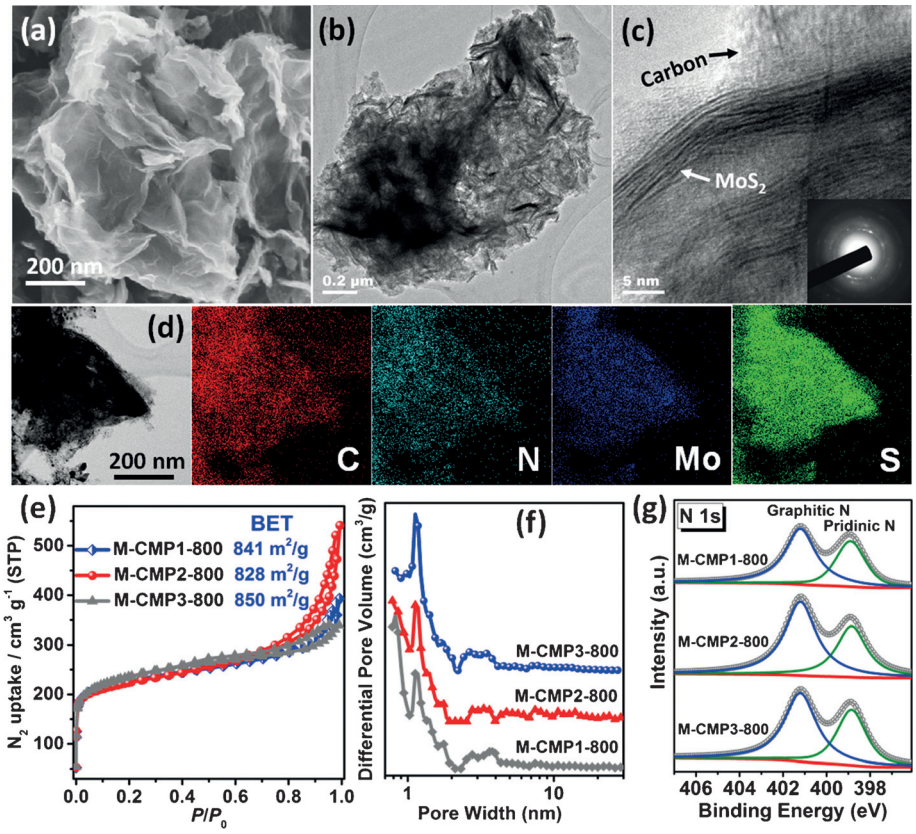

Figure 2. Characterization of MoS_2-based porous carbon nanosheets. a) SEM, b) TEM, and c) HRTEM images of M-CMP2-800. Inset of (c) shows the corresponding SAED pattern. d) STEM image of M-CMP2-800 and corresponding elemental mapping images for C, N, Mo and S. e) Nitrogen adsorption/desorption isotherms and corresponding BET surface areas. f) Pore size distributions of M-CMP1-800, M-CMP2-800, and M-CMP3-800. g) N1s core level XPS spectra of M-CMP1-800, M-CMP2-800, and M-CMP3-800.

that the pore structure is mainly preserved after pyrolysis (Figures 2e and S18). Thereby, the surface areas of the MoS_2-templated hybrids are higher than those of the corresponding porous carbons (681–828 $m^2 g^{-1}$) derived from the MoS_2-free CMPs thus demonstrating the advantages of MoS_2 templating strategy (Figures S19, S20 and Table S2). The large gas uptake at low relative pressure (below $p/p_0 = 0.1$) and the hysteretic loops in the high p/p_0 region of the isotherms indicate the coexistence of micro- and mesopores in the M-CMPs-*T* hybrids.[16] The peaks for diameters around 1.1 and 3.5 nm in the pore size distribution profiles (Figures 2f and S18) further confirm the hierarchical porous structure. Such large specific surface areas together with the hierarchical porous structure are crucial for accelerating electron- and mass-transport for device related applications, such as electrochemically catalyzed ORR and supercapacitors.

In the Raman spectra of M-CMPs-*T* (Figure S21), the MoS_2-related part (300–500 cm^{-1}) and two peaks around 1330 and 1590 cm^{-1} assigned to disordered (D-band) and ordered graphitic carbons (G-band), respectively, are clearly observed for all hybrids.[17] The observed relatively high intensity of the D-band (I_D/I_G ratio: ca. 1.2) for all M-CMPs-*T* hybrids can be attributed to disorder associated with edge defects.[13a,18] The introduction of nitrogen centers into the porous carbons also contributes to the D-band intensity.[13a] XPS measurements were carried out for identifying the elemental components of M-CMPs-*T* hybrids. Based on the XPS analysis (Figures 2g and S22), pyridinic and graphitic N were found at a nominal nitrogen level of 2.8, 3.6 and 3.1 wt% for M-CMP1-800, M-CMP2-800 and M-CMP3-800, respectively (Table S3). The pyridinic and graphitic nitrogen doping leads to a redistribution of charge and spin density of the adjacent carbons, which is also favorable for carbon-based energy storage/conversion, for example, ORR or supercapacitors.[13a,19]

Based on the above discussed hierarchical porous structure, their heteroatom-doping feature and 2D morphology, M-CMPs-*T* are promising candidates for electrochemically catalyzed ORR. The ORR activity of M-CMPs-*T* was studied under alkaline condition (0.1 M KOH). A scheme depicting of the ORR process at the M-CMPs-*T* hybrids is shown in Figure 3a, with the active sites homogeneously distributed throughout the M-CMPs-*T* nanosheets. O_2 molecules can be directly reduced into OH^- at the active sites. Cyclic voltammetry (CV) revealed a well-defined cathodic ORR peak for all the M-CMPs-*T* hybrids in O_2-saturated solutions in contrast to N_2-saturated solutions, indicating a pronounced catalytic activity of the hybrids. Thereby, M-CMP2-800 exhibited the highest peak current density at most positive potential (−0.21 V versus Ag/AgCl) in comparison with other 2D hybrids (Figures 3b and S23) and CMP2-800 (Figure S24).

To gain further insight into the ORR process, linear sweep voltammetry (LSV) measurements were recorded on the rotating disk electrode (RDE). Based on the LSV curves under a rotation of 1600 rpm (Figures S25–S27), the diffusion-limited currents at −0.6 V were 5.5, 4.7, 5.4, and 3.4 mA cm^{-2} for commercial Pt/C, M-CMP1-800, M-CMP2-800 and M-CMP3-800, respectively. M-CMP2-800 again showed the highest diffusion-limited current and the most positive onset

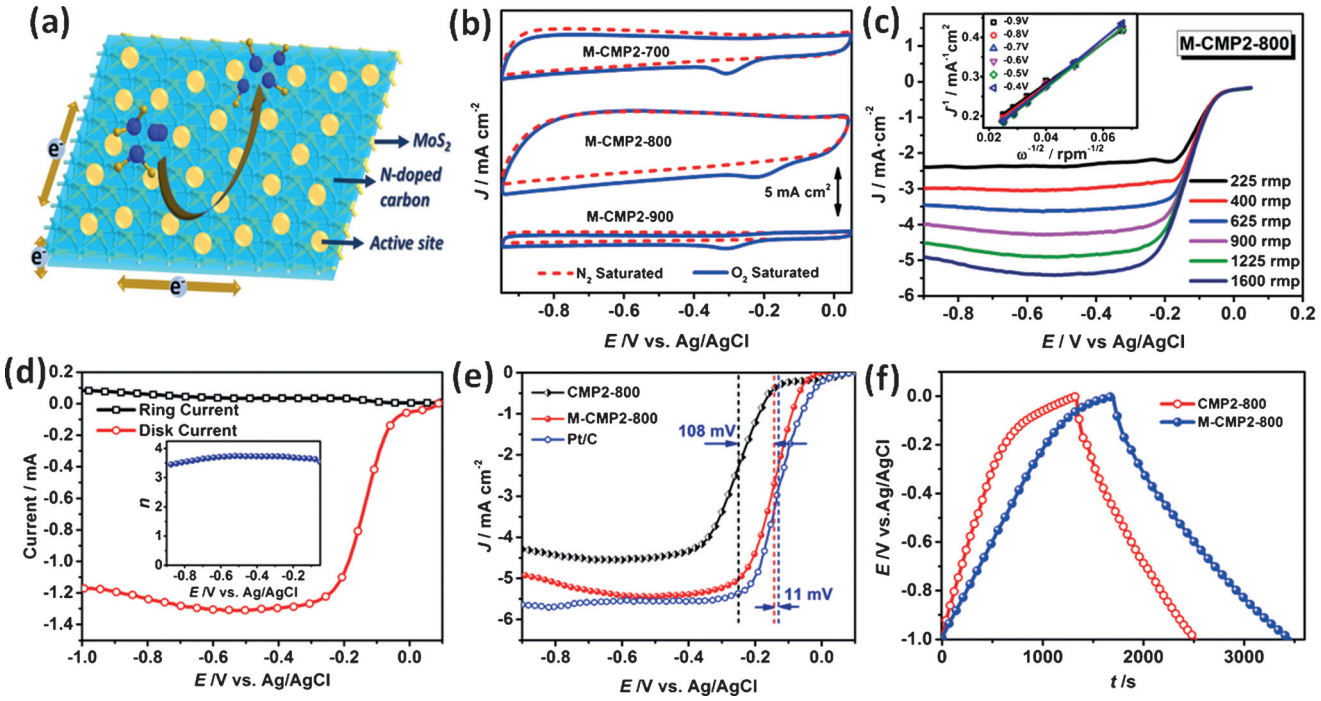

Figure 3. a) ORR process taking place at the surface of the M-CMPs-*T* hybrids in alkaline condition. b) CV curves in N_2- and O_2-saturated 0.1 M KOH. c) LSV curves for M-CMP2-800 at different rotation rates in O_2-saturated 0.1 M KOH at 5 mV s^{-1}. The inset shows the Koutecky–Levich (K-L) plots. d) RRDE curve for M-CMP2-800 for a rotation speed of 1600 rpm (inset: calculated electron transfer number (*n*) against the potential). e) LSV curves for CMP2-800, M-CMP2-800, and Pt/C at 1600 rpm and a scan rate of 5 mV s^{-1}. f) Galvanostatic charge/discharge curves of CMP2-800 and M-CMP2-800 at a current density of 0.2 A g^{-1}.

potential among M-CMPs-*T* hybrids, possibly as a result of the high specific surface area and N content (3.6 wt%, Table S3).

The electron transfer number per oxygen molecule (n) for ORR was calculated based on the LSV curves at different rotation rates (400–1600 rpm) and potentials (−0.4--0.9 V) by using the Koutechy–Levich (K-L) equation[20] (Supporting Information). The K-L plots show a good linearity for all potentials (Figures 3c and S28, S29). The electron transfer number n is calculated as ca. 4.0 between −0.4 and −0.9 V for M-CMP2-800. Based on the rotating ring-disk electrode (RRDE) curves (Figure 3d) a similar value for n is calculated (ca. 3.8, inset of Figure 3d), which is higher than the values for M-CMP1-800 (3.6) and M-CMP3-800 (3.3). Additionally, M-CMP2-800 shown the lowest peroxide yield (Figure S30), suggesting that the ORR catalyzed by M-CMP2-800 is mainly dominated by a four-electron transfer pathway. From the intercept of the K-L plots, the kinetic current density J_k corrected for mass transport is calculated as 26.3 mA cm^{-2} for M-CMP2-800, which is also higher than the values for the other samples (19.2 mA cm^{-2} for M-CMP1-800 and 9.1 mA cm^{-2} for M-CMP3-800). The half-wave potential (HWP) of M-CMP2-800 occurred at −0.14 V, 108 mV lower than that for MoS_2-free CMP2-800 (Figure 3e), and only 11 mV higher than the value of commercial Pt/C, impressively demonstrating its high catalytic activity. M-CMP1-800 and M-CMP3-800 display a similar decrease of the HWP values (Figures S31–S33) in comparison with those of the MoS_2-free CMP1-800 (by 194 mV) and CMP3-800 (by 106 mV), respectively. These results indicate a lower energy consumption and operation voltage for M-CMPs-*T* hybrids in comparison with corresponding MoS_2-free counterparts.

MoS_2-based materials can efficiently store charges by formation of intersheet and intrasheet double-layers or pseudocapacitances (faradaic charge-transfer process on the Mo center).[21] Regarding this point, M-CMPs-*T* hybrids have also been examined as electrode materials of supercapacitors for electrochemical energy storage (Figure 3f). The capacitive performance was investigated by CV and galvanostatic charge/discharge (GCD) measurements (Figures 3f, S34 and S35, more detailed discussions are given in the Supporting Information). Near-rectangular shape CV curves were observed for M-CMP2-800, indicating an ideal capacitive behavior. Remarkably, the current density for M-CMP2-800 was higher than that for MoS_2-free CMP2-800, indicating the vital contribution of the MoS_2 layer to the increase of the capacitance. Based on the GCD curves, the specific gravimetric capacitance of M-CMP2-800 was calculated to be 344 F g^{-1} at 0.2 A g^{-1}, 45% higher than the capacitance of CMP2-800 (237 F g^{-1}). The specific capacitance of M-CMP2-800 outperforms the values for other MoS_2-based electrodes, such as metallic 1T phase MoS_2,[22] hollow MoS_2 nanospheres[23] and MoS_2/graphene,[21a,24] and is comparable to the performance of heteroatom-doped graphene and porous carbon-based electrodes[3d,13a] (Table S4). The superior ORR and supercapacitor performances of M-CMPs-*T* hybrids should be significantly associated with a maximized synergistic interaction between MoS_2 and porous carbon layers combined with the presence of a hierarchical porous structure, providing channels for effective mass transport, and thus facilitating electrolyte penetration and ion diffusion.

In conclusion, a series of sandwich-like MoS_2-templated conjugated microporous polymer nanosheets (M-CMPs) with high specific surface area and aspect ratio was successfully developed by utilizing 4-iodophenyl-functionalized MoS_2 as template. By direct pyrolysis, 2D MoS_2/nitrogen-doped porous carbon (M-CMPs-*T*) hybrids were obtained with large specific surface areas and hierarchical porous structure. In these hybrids, both sides of the single-layer MoS_2 nanosheets were uniformly decorated with the nitrogen-doped porous carbon layers for good interfacial contact. The M-CMPs-*T* hybrids have been used for electrochemical catalyzed ORR with high activity and selectivity as well as for the construction of excellently performing supercapacitors. We expect that our novel strategy can be extended for the generation of various other layered hybrid materials for energy conversion and storage.

Acknowledgements

K.Y. and X.Z. would like to thank the fellowship program of the China Scholarship Council for financial support. The authors thank the Natural Science Foundation of China (51403126), the ERC (grant 2DMATER), and the EU Graphene Flagship program for financial support.

Keywords: conjugated microporous polymers · hybrid materials · molybdenum disulfide · noble-metal-free electrocatalysts · supercapacitors

How to cite: *Angew. Chem. Int. Ed.* **2016**, *55*, 6858–6863
Angew. Chem. **2016**, *128*, 6972–6977

[1] K. S. Novoselov, A. K. Geim, S. V. Morozov, D. Jiang, Y. Zhang, S. V. Dubonos, I. V. Grigorieva, A. A. Firsov, *Science* **2004**, *306*, 666–669.

[2] a) J. R. Lomeda, C. D. Doyle, D. V. Kosynkin, W.-F. Hwang, J. M. Tour, *J. Am. Chem. Soc.* **2008**, *130*, 16201–16206; b) E. Bekyarova, M. E. Itkis, P. Ramesh, C. Berger, M. Sprinkle, W. A. de Heer, R. C. Haddon, *J. Am. Chem. Soc.* **2009**, *131*, 1336–1337; c) K. Yuan, Y. Xu, J. Uihlein, G. Brunklaus, L. Shi, R. Heiderhoff, M. Que, M. Forster, T. Chasse, T. Pichler, T. Riedl, Y. Chen, U. Scherf, *Adv. Mater.* **2015**, *27*, 6714–6721; d) J. Greenwood, T. H. Phan, Y. Fujita, Z. Li, O. Ivasenko, W. Vanderlinden, H. Van Gorp, W. Frederickx, G. Lu, K. Tahara, Y. Tobe, I. H. Uji, S. F. Mertens, S. De Feyter, *ACS Nano* **2015**, *9*, 5520–5535; e) A. Criado, M. Melchionna, S. Marchesan, M. Prato, *Angew. Chem. Int. Ed.* **2015**, *54*, 10734–10750; *Angew. Chem.* **2015**, *127*, 10882–10900.

[3] a) K. Yuan, P. Guo-Wang, T. Hu, L. Shi, R. Zeng, M. Forster, T. Pichler, Y. Chen, U. Scherf, *Chem. Mater.* **2015**, *27*, 7403–7411; b) S. Liu, P. Gordiichuk, Z. S. Wu, Z. Liu, W. Wei, M. Wagner, N. Mohamed-Noriega, D. Wu, Y. Mai, A. Herrmann, K. Mullen, X. Feng, *Nat. Commun.* **2015**, *6*, 8817; c) M. Jahan, Q. Bao, J.-X. Yang, K. P. Loh, *J. Am. Chem. Soc.* **2010**, *132*, 14487–14495; d) X. Zhuang, F. Zhang, D. Wu, N. Forler, H. Liang, M. Wagner, D. Gehrig, M. R. Hansen, F. Laquai, X. Feng, *Angew. Chem. Int. Ed.* **2013**, *52*, 9668–9672; *Angew. Chem.* **2013**, *125*, 9850–9854; e) X. Zhuang, F. Zhang, D. Wu, X. Feng, *Adv. Mater.* **2014**, *26*, 3081–3086.

[4] a) X. Chia, A. Y. Eng, A. Ambrosi, S. M. Tan, M. Pumera, *Chem. Rev.* **2015**, *115*, 11941 – 11966; b) G. R. Bhimanapati, Z. Lin, V. Meunier, Y. Jung, J. Cha, S. Das, D. Xiao, Y. Son, M. S. Strano, V. R. Cooper, L. Liang, S. G. Louie, E. Ringe, W. Zhou, S. S. Kim, R. R. Naik, B. G. Sumpter, H. Terrones, F. Xia, Y. Wang, J. Zhu, D. Akinwande, N. Alem, J. A. Schuller, R. E. Schaak, M. Terrones, J. A. Robinson, *ACS Nano* **2015**, *9*, 11509 – 11539; c) H. Zhang, *ACS Nano* **2015**, *9*, 9451 – 9469; d) A. Gupta, T. Sakthivel, S. Seal, *Prog. Mater. Sci.* **2015**, *73*, 44 – 126.

[5] R. Lv, H. Terrones, A. L. Elías, N. Perea-López, H. R. Gutiérrez, E. Cruz-Silva, L. P. Rajukumar, M. S. Dresselhaus, M. Terrones, *Nano Today* **2015**, *10*, 559 – 592.

[6] S. Presolski, M. Pumera, *Mater Today* **2016**, *19*, 140 – 145.

[7] K. C. Knirsch, N. C. Berner, H. C. Nerl, C. S. Cucinotta, Z. Gholamvand, N. McEvoy, Z. Wang, I. Abramovic, P. Vecera, M. Halik, S. Sanvito, G. S. Duesberg, V. Nicolosi, F. Hauke, A. Hirsch, J. N. Coleman, C. Backes, *ACS Nano* **2015**, *9*, 6018 – 6030.

[8] T. Liu, C. Wang, X. Gu, H. Gong, L. Cheng, X. Shi, L. Feng, B. Sun, Z. Liu, *Adv. Mater.* **2014**, *26*, 3433 – 3440.

[9] D. Voiry, A. Goswami, R. Kappera, C. D. C. Castro e Silva, D. Kaplan, T. Fujita, M. Chen, T. Asefa, M. Chhowalla, *Nat. Chem.* **2015**, *7*, 45 – 49.

[10] E. P. Nguyen, B. J. Carey, J. Z. Ou, J. van Embden, E. D. Gaspera, A. F. Chrimes, M. J. S. Spencer, S. Zhuiykov, K. Kalantar-zadeh, T. Daeneke, *Adv. Mater.* **2015**, *27*, 6225 – 6229.

[11] a) H. Tang, J. Wang, H. Yin, H. Zhao, D. Wang, Z. Tang, *Adv. Mater.* **2015**, *27*, 1117 – 1123; b) H. Jiang, D. Ren, H. Wang, Y. Hu, S. Guo, H. Yuan, P. Hu, L. Zhang, C. Li, *Adv. Mater.* **2015**, *27*, 3687 – 3695.

[12] a) R. Silva, D. Voiry, M. Chhowalla, T. Asefa, *J. Am. Chem. Soc.* **2013**, *135*, 7823 – 7826; b) Y. Meng, D. Voiry, A. Goswami, X. Zou, X. Huang, M. Chhowalla, Z. Liu, T. Asefa, *J. Am. Chem. Soc.* **2014**, *136*, 13554 – 13557; c) S. Chen, J. Bi, Y. Zhao, L. Yang, C. Zhang, Y. Ma, Q. Wu, X. Wang, Z. Hu, *Adv. Mater.* **2012**, *24*, 5593 – 5597; d) J. Wei, Y. X. Hu, Y. Liang, B. A. Kong, J. Zhang, J. C. Song, Q. L. Bao, G. P. Simon, S. P. Jiang, H. T. Wang, *Adv. Funct. Mater.* **2015**, *25*, 5768 – 5777; e) S. Yang, L. Zhi, K. Tang, X. Feng, J. Maier, K. Müllen, *Adv. Funct. Mater.* **2012**, *22*, 3634 – 3640.

[13] a) Z. Xiang, D. Cao, L. Huang, J. Shui, M. Wang, L. Dai, *Adv. Mater.* **2014**, *26*, 3315 – 3320; b) Z.-S. Wu, L. Chen, J. Liu, K. Parvez, H. Liang, J. Shu, H. Sachdev, R. Graf, X. Feng, K. Müllen, *Adv. Mater.* **2014**, *26*, 1450 – 1455; c) L. Hao, S. Zhang, R. Liu, J. Ning, G. Zhang, L. Zhi, *Adv. Mater.* **2015**, *27*, 3190 – 3195.

[14] a) Y. Xu, S. Jin, H. Xu, A. Nagai, D. Jiang, *Chem. Soc. Rev.* **2013**, *42*, 8012 – 8031; b) L. Hao, J. Ning, B. Luo, B. Wang, Y. Zhang, Z. Tang, J. Yang, A. Thomas, L. Zhi, *J. Am. Chem. Soc.* **2015**, *137*, 219 – 225; c) Z. Xiang, Y. Xue, D. Cao, L. Huang, J.-F. Chen, L. Dai, *Angew. Chem. Int. Ed.* **2014**, *53*, 2433 – 2437; *Angew. Chem.* **2014**, *126*, 2465 – 2469.

[15] X. Zhuang, D. Gehrig, N. Forler, H. Liang, M. Wagner, M. R. Hansen, F. Laquai, F. Zhang, X. Feng, *Adv. Mater.* **2015**, *27*, 3789 – 3796.

[16] R. Du, N. Zhang, H. Xu, N. Mao, W. Duan, J. Wang, Q. Zhao, Z. Liu, J. Zhang, *Adv. Mater.* **2014**, *26*, 8053 – 8058.

[17] A. C. Ferrari, J. C. Meyer, V. Scardaci, C. Casiraghi, M. Lazzeri, F. Mauri, S. Piscanec, D. Jiang, K. S. Novoselov, S. Roth, A. K. Geim, *Phys. Rev. Lett.* **2006**, *97*, 187401.

[18] A. C. Ferrari, D. M. Basko, *Nat. Nanotechnol.* **2013**, *8*, 235 – 246.

[19] H.-W. Liang, X. Zhuang, S. Brüller, X. Feng, K. Müllen, *Nat. Commun.* **2014**, *5*, 4973.

[20] Y. Liang, Y. Li, H. Wang, J. Zhou, J. Wang, T. Regier, H. Dai, *Nat. Mater.* **2011**, *10*, 780 – 786.

[21] a) E. G. da Silveira Firmiano, A. C. Rabelo, C. J. Dalmaschio, A. N. Pinheiro, E. C. Pereira, W. H. Schreiner, E. R. Leite, *Adv. Energy Mater.* **2014**, *4*, 1301380; b) G. Sun, X. Zhang, R. Lin, J. Yang, H. Zhang, P. Chen, *Angew. Chem. Int. Ed.* **2015**, *54*, 4651 – 4656; *Angew. Chem.* **2015**, *127*, 4734 – 4739.

[22] M. Acerce, D. Voiry, M. Chhowalla, *Nat. Nanotechnol.* **2015**, *10*, 313 – 318.

[23] L. Wang, Y. Ma, M. Yang, Y. Qi, *Electrochim. Acta* **2015**, *186*, 391 – 396.

[24] Q. Mahmood, S. K. Park, K. D. Kwon, S.-J. Chang, J.-Y. Hong, G. Shen, Y. M. Jung, T. J. Park, S. W. Khang, W. S. Kim, J. Kong, H. S. Park, *Adv. Energy Mater.* **2016**, *6*, 1501115.

Received: January 26, 2016
Published online: April 21, 2016

